Nanoscale

PAPER

View Article Online
View Journal | View Issue

Cite this: *Nanoscale*, 2021, **13**, 4569

CoP_2/Fe-CoP_2 yolk–shell nanoboxes as efficient electrocatalysts for the oxygen evolution reaction†

Vinoth Ganesan, Jihye Son and Jinkwon Kim *

Received 13th November 2020,
Accepted 29th January 2021

DOI: 10.1039/d0nr08108f

rsc.li/nanoscale

The development of an efficient electrocatalyst is an important requirement for water splitting systems to produce clean and sustainable hydrogen fuel. Herein, we synthesized CoP_2/Fe-CoP_2 yolk–shell nanoboxes (YSBs) as efficient electrocatalysts for the oxygen evolution reaction (OER). Initially, zeolitic imidazolate framework-67/CoFe-Prussian blue analogue (ZIF-67/CoFe-PBA) YSBs were prepared by the reaction of ZIF-67 and $[Fe(CN)_6]^{3-}$ ions in the presence of a small amount of water as an etching agent. The size of the CoP_2 yolk depends on the amount of water. The heteronanostructure composed of the CoP_2 yolk and the $Fe_xCo_{1-x}P_2$ shell with a cubic shape was obtained by phosphidation of ZIF-67/CoFe-PBA YSBs. Benefiting from the unique structure and chemical composition, the CoP_2/Fe-CoP_2 YSB electrocatalyst has a large specific surface area of 114 $m^2\ g^{-1}$ and shows superior electrocatalytic performances for the OER such as a low overpotential of 266 mV, a small Tafel slope value of 68.1 mV dec^{-1}, and excellent cyclic stability.

1. Introduction

Electrochemical water splitting is a sustainable and environmentally friendly approach to producing clean hydrogen fuel.[1] The development of active electrocatalysts for the oxygen evolution reaction (OER) is critical to promoting commercial applications of hydrogen fuel cells. The OER, the half reaction of the water splitting reaction at the anode, is a four-electron transfer reaction, which requires high energy to overcome the kinetic barrier of the reaction. Therefore, in the past several decades, many efforts have been devoted to develop an efficient OER catalyst to improve electrode kinetics and stability in acid and alkaline solutions.[2–4] RuO_2 and IrO_2 catalysts are known to be the most active catalysts for the OER.[5,6] However, their high cost and low natural abundance limit their commercial use.[7] Alternatively, transition metal oxides, chalcogenides, carbides, nitrides and phosphides have been explored to replace the precious metal based OER catalysts.[8–13]

Transition metal phosphides have recently emerged as Earth-abundant catalysts for the overall water splitting process.[14] In particular, cobalt phosphides with various stoichiometric ratios (CoP, Co_2P, CoP_2) have attracted much attention in the research field of the OER.[15–17] According to the recent theoretical and experimental studies, the catalytic activity of CoP_2 is superior to those of CoP and Co_2P.[18] The positively charged cobalt ions serve as hydroxyl receptors and the negatively charged P atoms facilitate the desorption of O_2 molecules. Wang *et al.* investigated for the first time the electrocatalytic OER performance of CoP_2 nanoparticles on reduced graphene oxide sheets.[19] Furthermore, the use of bimetallic phosphides obtained by the doping of other transition metal atoms improves the electrocatalytic performance by optimizing the electronic structure and surface energy of the catalysts.[20]

Morphology control is another effective way to further improve the electrochemical performances of the catalysts.[21–25] Among hollow nanostructures, the yolk–shell structure has been found to be one of the most efficient structures for electrocatalysts.[26] The large specific surface area of hollow yolk–shell structures can provide more active sites for redox reactions. Yin *et al.* reported the synthesis of $Ni_xCo_{1-x}P$ yolk–shell spheres showing high activity and stability for overall water splitting.[27] Metal–organic frameworks (MOFs) can provide a variety of possibilities to prepare unique hollow materials with well-defined interior voids, a large surface area, a low density, and abundant active sites.[28,29] He *et al.* reported MOF-derived synthesis of carbon-incorporated nickel–cobalt mixed metal phosphide (NiCoP/C) nanoboxes by a reaction of ZIF-67 nanocubes with $Ni(NO_3)_2$.[30] Furthermore, Prussian blue analogues (PBAs) have emerged as useful precursors for the synthesis of

Department of Chemistry, Kongju National University, 56 Gongjudaehak-ro, Gongju-si, Chungnam-do, 32588, Republic of Korea. E-mail: jkim@kongju.ac.kr; Fax: +82-41-850-8613; Tel: +82-41-850-8496

†Electronic supplementary information (ESI) available: XRD pattern and SEM image of ZIF-67. The XRD pattern of ZIF-67/CoFe-PBA YSBs. The EDS spectrum of CoP_2/Fe-CoP_2 YSBs and Fe-CoP_2 NBs. The OER stability curves of Fe-CoP_2 NBs and the cyclic voltammetry curves of Fe-CoP_2 NBs and CoP_2 NCs. The SEM images of CoP_2/Fe-CoP_2 YSBs after the durability test. See DOI: 10.1039/d0nr08108f

hollow nanostructures for energy storage and conversion applications.[31–34]

Herein, we demonstrate the rational design and synthesis of CoP_2/Fe-CoP_2 yolk–shell nanoboxes by the formation of the cobalt iron ferricyanide (CoFe-PBA) structure on sacrificial ZIF-67. CoP_2/Fe-CoP_2 YSBs exhibited excellent electrocatalytic activity for the OER, in terms of low overpotential and low Tafel slope values with long time cyclic stability.

2. Experimental

2.1. Materials

$Co(NO_3)_2{\cdot}6H_2O$ (98%), 2-methylimidazole (99%), cetyltrimethylammonium bromide (CTAB) (98%), $K_3[Fe(CN)_6]$ (99%), Nafion solution (5 wt%) and NaH_2PO_2 (99.99%) (Sigma-Aldrich). Ethanol and propanol (Samchun Chemicals).

2.2. Synthesis of ZIF-67/CoFe-PBA YSBs

ZIF-67 nanocube (NC) particles were prepared according to a previous report.[35] A solution of 44 mg of ZIF-67 NCs in 30 mL of ethanol was sonicated for 10 minutes and mixed with a solution of 100 mg of $K_3[Fe(CN)_6]$ in 10 mL of water at 50 °C. After stirring for 1 hour, the solid product was separated, washed several times with ethanol, and dried under reduced pressure at room temperature. To prepare ZIF-67/CoFe-PBA NBs, 15 mL of water was used in the reaction mixture.

2.3. Synthesis of CoP_2/Fe-CoP_2 YSBs

The solid sample of ZIF-67/CoFe-PBA YSBs (30 mg) was heated at 300 °C with a heating rate of 2 °C min^{-1} in the presence of NaH_2PO_2 (150 mg) under an Ar gas flow for 2 h to afford the product. The same process was applied to prepare Fe-CoP_2 nanoboxes (NBs).

2.4. Characterization

X-ray diffraction (XRD) measurements were performed to characterize the crystal structure of the product (Rigaku, X-MAX 2000-PC). The morphology and composition of the synthesized nanocrystals were characterized by field emission scanning electron microscopy (FESEM, Hitachi HF-4800), transmission electron microscopy (TEM), and high-resolution TEM (JEM-ARM200F, JEOL, acceleration voltage: 200 kV). The surface area and pore size distribution were determined using an ASAP-2420 (Micromeritics, USA). X-ray photoelectron spectroscopy (XPS) was conducted to characterize the chemical and valency states of the products.

2.5. Electrochemical measurements

Electrochemical investigation of the products was conducted in a three electrode configuration in 1 M KOH using PGSTAT 302N Autolab (Metrohm) – the working electrode (glassy carbon of 3 mm diameter), reference electrode (Ag/AgCl; saturated KCl) and counter electrode (graphite rod). 2 mg of catalyst was dispersed in 200 μL solution (isopropanol: 190 μL and 5 wt% Nafion: 10 μL) and sonicated for 20 min. Then, 2 μL of the catalyst ink was loaded on the glassy carbon and then dried at ambient temperature. The average loading of the catalyst was about 0.21 mg cm^{-2}. The stability test was performed at a constant overpotential (*vs.* RHE). Cyclic voltammetry (CV, scan rate: 10 mV s^{-1}) was conducted to measure the double-layer capacitance (C_{dl}). Impedance analyses were performed in the frequency range of 0.1 Hz to 100 Hz (ZIVA-MP2A).

3. Results and discussion

The synthesis procedure of CoP_2/Fe-CoP_2 YSBs is schematically illustrated in Scheme 1. ZIF-67 nanocrystals with the average size of 500 nm were synthesized by a surfactant assisted hydrothermal method (Fig. S1†).[35] Cobalt ferricyanide (CoFe-PBA) was formed on the sacrificial ZIF-67 NCs by the reaction of $Fe(CN)_6^{3-}$ anions and Co_2^{+} cations released from ZIF-67 NCs to form the Co-ZIF/CoFe-PBA yolk–shell structure. CoP_2/Fe-CoP_2 YSBs were obtained by direct phosphidation under an anaerobic atmosphere.

Fig. 1 shows the FESEM and TEM images of ZIF-67/CoFe-PBA YSBs with the average size of ~500 nm. Fig. 1b shows the yolk–shell particle composed of a solid core and an outer shell comprising small nanograins. According to the elemental mapping analysis, the Co element is uniformly distributed in both the yolk and shell, whereas Fe is observed only in the outer shell of the nanobox (Fig. 1c). Fig. S2† shows the XRD pattern of ZIF-67/CoFe-PBA YSBs. Along with the XRD peaks of ZIF-67, two characteristic peaks were also observed at 25.0° and 35.5° due to the (002) and (400) planes of Co–Fe PBA, which proves the formation of the hybrid MOF structure.

Water promotes the ion exchange reaction of ZIF-67 NCs and $K_3[Fe(CN)_6]$. The morphology of YSBs can be controlled by changing the water/ethanol ratio. In a condition of 5 mL water and 25 mL ethanol, the size of ZIF-67 crystals reduces slightly and the CoFe-PBA shell begins to appear (Fig. 2a). Increasing the amount of water to 10 mL makes the ZIF-67 cube smaller and results in a cubic yolk–shell structure (Fig. 2b). The ZIF-67 yolk disappears by adding more water (Fig. 2c). Water dissolves ZIF-67 crystals and the released Co_2^{+} cations react with $[Fe(CN)_6]^{3-}$ anions to form a cubic shell, *i.e.*, the etching of ZIF-67 crystals and the formation of Co–Fe PBA occur simultaneously. The shrinkage and collapse of the nanobox structure were observed with 20 mL of water (Fig. 2d).

CoP_2/Fe-CoP_2 YSBs were synthesized by a direct phosphidation process. Fig. 3 shows the XRD pattern of the product and

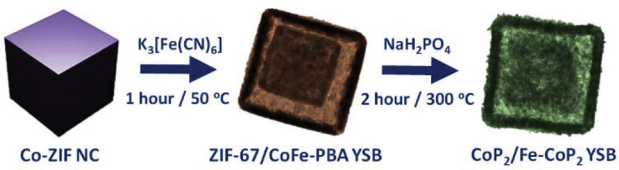

Scheme 1 Schematic representation for the synthesis of CoP_2/Fe-CoP_2 YSB catalysts.

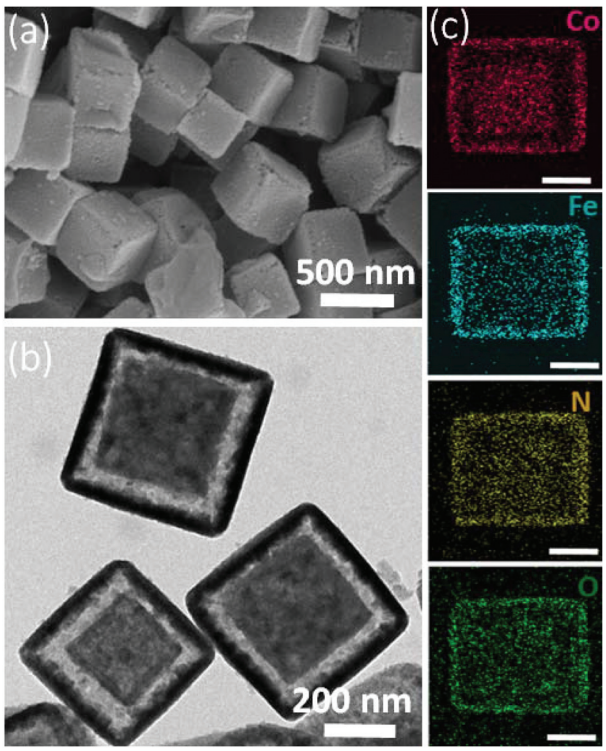

Fig. 1 (a) SEM and (b) TEM images of ZIF-67/CoFe-PBA YSBs. (c) Corresponding mapping images (scale bar: 200 nm).

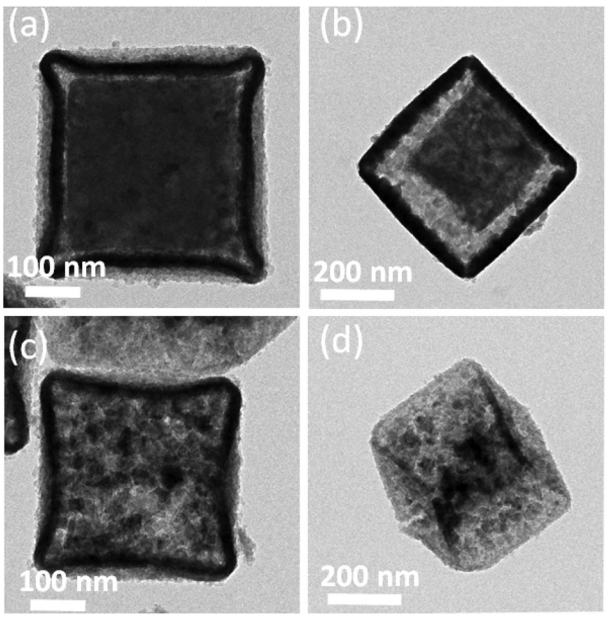

Fig. 2 TEM images observed under different reaction conditions. (a) 5 mL (b) 10 mL (c) 15 mL and (d) 20 mL of water.

the main diffraction peaks can be assigned to monoclinic CoP_2 (JCPDS no. #77-0263).

The shape and size of the yolk–shell structure were retained without noticeable changes even after phosphidation with the

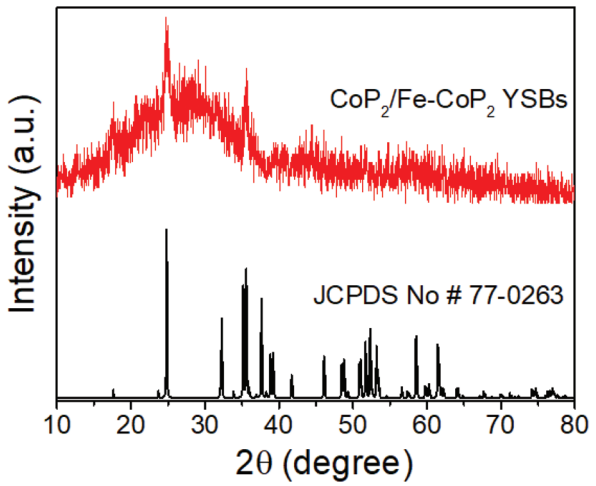

Fig. 3 XRD pattern of CoP_2/Fe-CoP_2 YSBs.

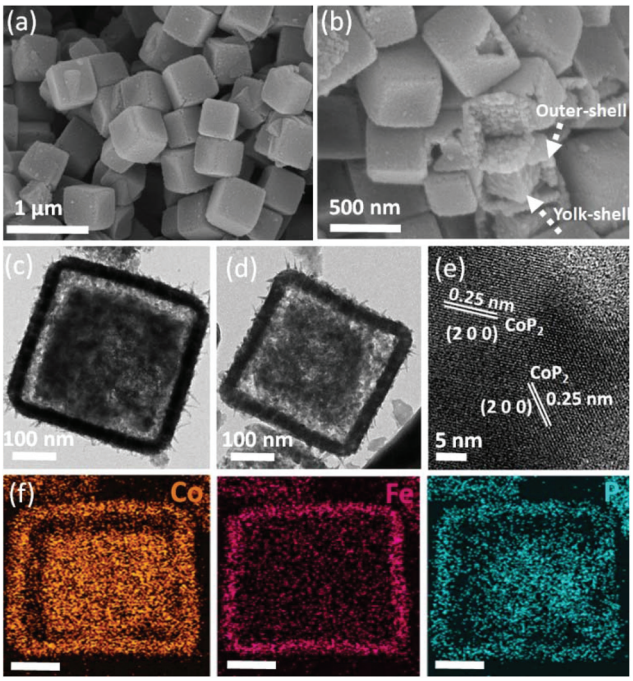

Fig. 4 (a and b) SEM and (c and d) TEM images of CoP_2/Fe-CoP_2 YSBs. (e) Corresponding HR-TEM image and (f) STEM mapping images (scale bar: 100 nm).

average size of 500 nm (Fig. 4a). Broken particles clearly show that the outer shell of a particle is comprised of tiny nano-sized particles (Fig. 4b). Fig. 4c and d show the TEM images of yolk–shell particles, which are in full consistency with the SEM results. The lattice fringe spacing of 0.25 nm corresponds to the (200) plane of CoP_2 (Fig. 4e). STEM mapping analysis reveals that Co, Fe, and P elements are evenly distributed. Co and P are found throughout the particle, but Fe is found at the outer shell (Fig. 4f). The elemental composition of Fe/Co/P was observed to be 0.27 : 0.73 : 2, being consistent with the

stoichiometry of transition metal diphosphides (MP_2) (Fig. S3†). Furthermore, the relative amounts of CoP_2 and Fe-CoP_2 of CoP_2/Fe-CoP_2 YSBs could be estimated by measuring the dimensions of a single hybrid particle. The calculated mass percentages of Fe-CoP_2 and CoP_2 are about 61% and 39%, respectively, suggesting that the atomic ratio of Fe and Co is about 1 : 1.26.

The Brunauer–Emmett–Teller (BET) specific surface area was found to be 114 $m^2\ g^{-1}$ with a pore size distribution of 11–19 nm, indicating that the yolk–shell particles have a large surface area and are of mesoporous nature (Fig. 5a). The chemical valence states of the elements were characterized by XPS analyses. The spin–orbit doublets of Co $2p_{3/2}$ and Co $2p_{1/2}$ observed at 781.2 and 794.1 eV, respectively, in the Co 2P spectrum (Fig. 5b) can be consistent with those of the spectrum of $FeCoP_2$ nanowires.[36] Additional doublets at 786.2 and 803.8 eV are attributed to the oxidized Co.[36,37] The Fe 2p spectrum (Fig. 5c) exhibits two distinct peaks located at 708.9 and 722.1 eV, reflecting the binding energies of Fe^{2+} $2p_{3/2}$ and Fe^{2+} $2p_{1/2}$, respectively. The second doublets at 711.5 eV and 724.5 eV are due to Fe^{3+}.[36,37] Fig. 5d shows the P 2p spectrum consisting of two characteristic peaks at 129.1 eV for P $2p_{3/2}$ and a relatively broader peak at 133.7 eV for the P–O species due to surface oxidation.[38]

The TEM images of Fe-CoP_2 NBs are shown in Fig. 6. The surface of the nanoboxes is composed of small nanograins. The obtained lattice fringe value of 0.25 nm corresponds to the (2 0 0) plane of CoP_2 (Fig. 6b). The XRD pattern and elemental composition of Fe-CoP_2 NBs are shown in Fig. S4 and S5.† The obtained diffraction peaks are well matched with monoclinic CoP_2 (JCPDS no. #77-0263). The elemental composition of Fe/Co/P of the Fe-CoP_2 nanobox is almost similar to that of CoP_2/Fe-CoP_2 YSBs (Fig. S5†). In addition, the elemental mapping image (Fig. 6c) shows that Co and P elements are

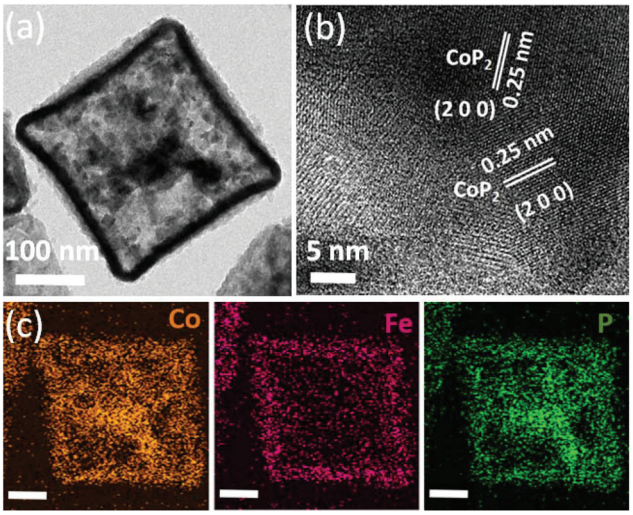

Fig. 6 (a) TEM image and (b) HR-TEM image of Fe-CoP_2 NBs. (c) Corresponding mapping images (scale bar: 100 nm).

relatively evenly distributed on the entire surface of the image, whereas Fe accumulated on the edge of the image. This suggests that the dissolved Co cations from the core part were deposited on the inner surface of the hollow box. Therefore, the total elemental ratio of Fe/Co/P does not seem to depend on the structural change during the reaction. Furthermore, CoP_2 nanocubes were synthesized by the phosphidation of ZIF-67 NCs for the comparison of the eletrocatalytic activity with that of yolk–shell particles. The XRD pattern and FESEM image of CoP_2 nanocubes are provided in Fig. S6.†

The polarization curve in Fig. 7a shows that CoP_2/Fe-CoP_2 YSBs exhibit a low overpotential (η_{10}) of 266 mV, whereas Fe-CoP_2 NBs need a slightly high overpotential (η_{10}) of 320 mV. These values are much lower than those of the IrO_2 bench-

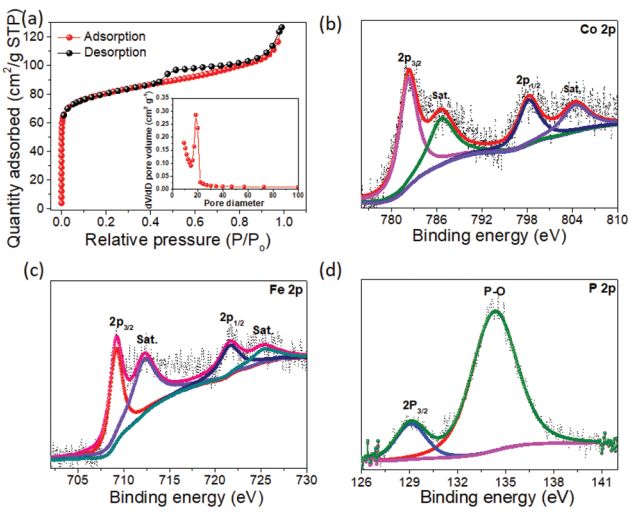

Fig. 5 (a) Nitrogen adsorption–desorption isotherm (the inset shows the pore size distribution curve) for CoP_2/Fe-CoP_2 YSBs. (b) High-resolution XPS spectra of Co 2p, (c) Fe 2p and (d) P 2p for CoP_2/Fe-CoP_2 YSBs.

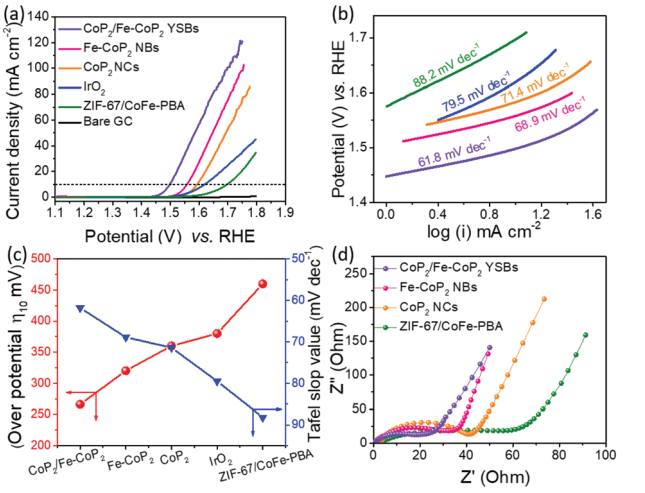

Fig. 7 (a) Linear sweep voltammetry curves of different electrocatalysts. (b) Corresponding Tafel slopes. (c) The required overpotential to achieve a current density of 10 mA cm^{-2} and Tafel slope values for different catalysts. (d) Corresponding EIS Nyquist plots.

mark catalyst (380 mV), CoP_2 NCs (360 mV), and ZIF-67/CoFe-PBA YSBs (460 mV). However, the yolk–shell nanobox catalyst exhibits a high current density of 50 mA cm^{-2} and 100 mA cm^{-2} at an overpotential (η_{10}) of 350 and 410 mV, respectively, which are higher than other catalysts. Additionally, the overpotential of CoP_2/Fe-CoP_2 YSBs is also significantly lower than the reported values of other catalysts, including NiCoP/C nanoboxes (300 mV),[30] $Co_{0.6}Fe_{0.4}P$ (298 mV),[32] AlCoP (330 mV),[39] CoP/carbon dots (400 mV),[40] $(Co_{0.54}Fe_{0.46})_2P$ (370 mV),[41] $Ni_{0.6}Co_{1.4}P$ nanocages (300 mV),[42] Fe–Co–P nanoboxes (269 mV),[43] and hollow $FeCo_2P$ (320 mV).[44] As shown in Fig. 7b, the measured Tafel slope of CoP_2/Fe-CoP_2 YSBs (61.8 mV dec^{-1}) is lower than those of Fe-CoP_2 NBs (68.9 mV dec^{-1}), CoP_2 NCs (71.4 mV dec^{-1}), IrO_2 (79.5 mV dec^{-1}) and ZIF-67/CoFe-PBA YSBs (88.2 mV dec^{-1}), implying that the CoP_2/Fe-CoP_2 YSB catalyst has faster OER kinetics. Fig. 7c shows the overpotential and the corresponding Tafel slope values of the catalysts. EIS measurement was carried out to demonstrate the charge transfer resistance (R_{ct}) of the catalysts (Fig. 7d). CoP_2/Fe-CoP_2 YSBs exhibited a lower R_{ct} value (18.3 Ω) than Fe-CoP_2 NBs (33.1 Ω), CoP_2 NCs (40.1 Ω), and ZIF-67/CoFe-PBA YSBs (57.8 Ω). The higher electrical conductivity of CoP_2/Fe-CoP_2 YSBs might be due to the hybrid yolk–shell structure, which promotes efficient charge transfer, prevents aggregation during the electrochemical reaction, and generates strong couple effects that result in enhanced electrocatalytic activity.[32,45]

The durability test was performed for CoP_2/Fe-CoP_2 YSBs using CV at a fixed scan rate of 10 mV s^{-1} (Fig. 8a). A slight overpotential increase (11 mV) was observed for CoP_2/Fe-CoP_2 YSBs, whereas Fe-CoP_2 NBs showed an overpotential increase of 17 mV after 3000 cycles (Fig. S7†). The chronoamperometry test was conducted at a static potential of 1.50 V (*vs.* RHE) (Fig. 8b). The current density of the CoP_2/Fe-CoP_2 YSB catalyst could be maintained even after electrolysis for 10 hours. The SEM image revealed that the yolk–shell structure was preserved well after the durability test (Fig. S8†), implying the robust nature of the catalysts.

As shown in Fig. S9,† *ex situ* XPS measurement was conducted to investigate the surface chemical composition of CoP_2/Fe-CoP_2 after the OER. The high resolution Co 2p XPS spectrum shows that the peaks at 780.3 and 795.6 eV are related to Co^{3+} and high resolution Fe 2p peaks at 709.5 and 722.6 eV are attributed to Fe^{3+}.[46–48] The binding energy of P 2p at 129.1 eV disappeared, which suggests the oxidation of the P centre on the surface of the catalyst. Therefore, the surface of the catalyst is oxidized into metal oxides or hydroxides during the OER under strong alkaline conditions, consistent with the previous reports.[43,49]

The electrochemically active surface area (ECSA) was determined using CV measurements for CoP_2/Fe-CoP_2 YSBs, Fe-CoP_2 NBs and CoP_2 NCs (Fig. 8c, S10a and S10b†). The anodic current densities measured at a fixed potential of 1.35 V (*vs.* RHE) are plotted with respect to scan rates in Fig. 8d. The capacitance of 19.43 mF cm^{-2} for CoP_2/Fe-CoP_2 YSBs is higher than those of Fe-CoP_2 NBs (15.17 mF cm^{-2}) and CoP_2 NCs (10.62 mF cm^{-2}), implying that the CoP_2/Fe-CoP_2 YSB catalyst shows a high double-layer capacitance and a high electrochemically active surface area because of the yolk–shell structure.

The superior electrocatalytic activity might be ascribed to the unique yolk–shell structure with a favourable chemical composition. CoP_2/Fe-CoP_2 YSBs composed of CoP_2 particles (core) and Fe-CoP_2 nanoboxes (shell) show a significantly lower overpotential than their ingredients. The presence of Fe, a unique yolk–shell structure, and the hollow nature of the catalyst are believed to contribute to enhancing the electrocatalytic activity for the OER. Particularly, a large electrochemical surface area and abundant electroactive sites of the yolk–shell structure can effectively shorten the diffusion length of ions and expose more active sites than solid counterparts.[50–52] In addition, the integrated nanostructure prevents the aggregation during continuous gas evolution.[53]

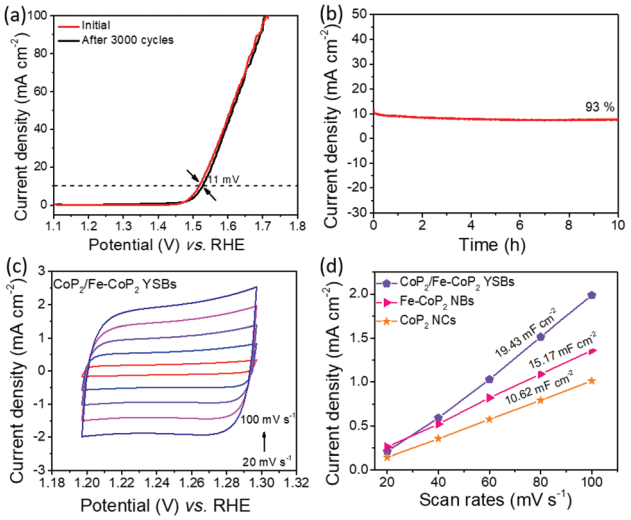

Fig. 8 (a) LSV curves of CoP_2/Fe-CoP_2 YSBs before and after 3000 cycles. (b) Chronoamperometry stability test at a static potential of 1.5 V (*vs.* RHE) for 10 hours. (c) Cyclic voltammetry curves of CoP_2/Fe-CoP_2 YSBs at different scan rates. (d) The capacitive current density as a function of scan rate for CoP_2/Fe-CoP_2 YSBs, Fe-CoP_2 NBs and CoP_2 NCs. The measured double-layer capacitance of the system is taken as the average of the absolute value of the slope of linear fits to the data.

3. Conclusions

In summary, we synthesized CoP_2/Fe-CoP_2 YSBs using hybrid MOFs as a promising electrocatalyst for the OER. The anion-exchange reaction and subsequent phosphidation process resulted in the formation of CoP_2/Fe-CoP_2 YSBs. The formation process of yolk–shell structures was observed systematically by TEM under different reaction conditions. Owing to the large surface area and many active sites, the CoP_2/Fe-CoP_2 YSB catalyst not only provides superior electrocatalytic OER performances such as low overpotential and small Tafel slope values, but also shows superior cyclic stability. This synthetic approach can be extended to produce a variety of metal phos-

phides with a hollow structure for energy storage and conversion applications.

Conflicts of interest

There are no conflicts to declare.

Acknowledgements

This work was supported by the National Research Foundation of Korea (NRF-2019R1F1A1059831).

References

1 H. Wang, H. W. Lee, Y. Dend, Z. Li, P. C. Hsu, Y. Li, D. Lin and Y. Cui, *Nat. Commun.*, 2015, **6**, 1.
2 N.-T. Suen, S.-F. Hung, Q. Quan, N. Zhang, Y.-J. Xu and H. M. Chen, *Chem. Soc. Rev.*, 2017, **46**, 337–365.
3 N. B. Halck, V. Petrykin, P. Krtil and J. Rossmeisl, *Phys. Chem. Chem. Phys.*, 2014, **16**, 13682–13688.
4 M. Tahira, L. Pana, F. Idrees, X. Zhang, L. Wang, J.-J. Zou and Z. L. Wang, *Nano Energy*, 2017, **37**, 136–157.
5 Y. Lee, J. Suntivich, K. J. May, E. E. Perry and Y. Shao-Horn, *J. Phys. Chem. Lett.*, 2012, **3**, 399–404.
6 T. Reier, M. Oezaslan and P. Strasser, *ACS Catal.*, 2012, **2**, 1765–1772.
7 Z. Cai, X. Bu, P. Wang, J. C. Ho, J. Yang and X. Wang, *J. Mater. Chem. A*, 2019, **7**, 5069–5089.
8 E. Fabbri, A. Habereder, K. Waltar, R. Kötz and T. J. Schmidt, *Catal. Sci. Technol.*, 2014, **4**, 3800–3821.
9 S. Anantharaj, S. R. Ede, K. Sakthikumar, K. Karthick, S. Mishra and S. Kundu, *ACS Catal.*, 2016, **6**, 8069–8097.
10 U. D. Silva, J. Masud, N. Zhang, Y. Hong, W. P. R. Liyanage, M. A. Zaeem and M. Nath, *J. Mater. Chem. A*, 2018, **6**, 7608–7622.
11 Y.-J. Tang, C.-H. Liu, W. Huang, X.-L. Wang, L.-Z. Dong, S.-L. Li and Y.-Q. Lan, *ACS Appl. Mater. Interfaces*, 2017, **9**, 16977–16985.
12 C. Liu, G. Bai, X. Tong, Y. Wang, B. Lv, N. Yang and X.-Y. Guo, *Electrochem. Commun.*, 2019, **98**, 87–91.
13 L. Ji, J. Wang, X. Teng, T. J. Meyer and Z. Chen, *ACS Catal.*, 2020, **10**, 412–419.
14 A. Parra-Puerto, K. L. Ng, K. Fahy, A. E. Goode, M. P. Ryan and A. Kucernak, *ACS Catal.*, 2019, **9**, 11515–11529.
15 H. Li, Q. Li, P. Wen, T. B. Williams, S. Adhikari, C. Dun, C. Lu, D. Itanze, L. Jiang, D. L. Carroll, G. L. Donati, P. M. Lundin, Y. Qiu and S. M. Geyer, *Adv. Mater.*, 2018, **30**, 1705796.
16 Y. Bai, H. Zhang, Y. Feng, L. Fang and Y. Wang, *J. Mater. Chem. A*, 2016, **4**, 9072–9079.
17 S. Yang, M. Xie, L. Chen, W. Wei, X. Lv, Y. Xu, N. Ullah, O. C. Judith, Y. B. Adegbemiga and J. Xie, *Int. J. Hydrogen Energy*, 2019, **44**, 4543–4552.
18 H. Li, P. Wen, D. S. Itanze, M. W. Kim, S. Adhikari, C. Lu, L. Jiang, Y. Qiu and S. M. Geyer, *Adv. Mater.*, 2019, **31**, 1900813.
19 J. Wang, W. Yangac and J. Liu, *J. Mater. Chem. A*, 2016, **4**, 4686–4690.
20 L. Wang, H. Wu, S. Xi, S. T. Chua, F. Wang, S. J. Pennycook, Z. G. Yu, Y. Du and J. Xue, *ACS Appl. Mater. Interfaces*, 2019, **11**, 17359–17367.
21 H. Mistry, A. S. Varela, S. Kühl, P. Strasser and B. R. Cuenya, *Nat. Rev.*, 2016, **1**, 16009.
22 Y. Guo, T. Park, J. W. Yi, J. Henzie, J. Kim, Z. Wang, B. Jiang, Y. Bando, Y. Sugahara, J. Tang and Y. Yamauchi, *Adv. Mater.*, 2019, **31**, 1807134.
23 S. Li, X. Hao, A. Abudulac and G. Guan, *J. Mater. Chem. A*, 2019, **7**, 18674–18707.
24 B. Wang, C. Tang, H.-F. Wang, X. Chen, R. Cao and Q. Zhang, *Adv. Mater.*, 2019, **31**, 1805658.
25 M. Li, X. Deng, Y. Liang, K. Xiang, D. Wu, B. Zhao, H. Yang, J.-L. Luo and X.-Z. Fu, *J. Energy Chem.*, 2020, **50**, 314–323.
26 Z. Li, M. Li, Z. Bian, Y. Kathiraser and S. Kawi, *Appl. Catal., B*, 2016, **188**, 324–341.
27 Z. Yin, C. Zhu, C. Li, S. Zhang, X. Zhang and Y. Chen, *Nanoscale*, 2016, **8**, 19129–19138.
28 X.-C. Xie, K.-J. Huang and X. Wu, *J. Mater. Chem. A*, 2018, **6**, 6754–6771.
29 V. Ganesan, P. Ramasamy and J. Kim, *Int. J. Hydrogen Energy*, 2017, **42**, 5985–59992.
30 P. He, X.-Y. Yu and X. W. Lou, *Angew. Chem., Int. Ed.*, 2017, **56**, 3897–3900.
31 C. Xuan, J. Wang, W. Xia, Z. Peng, Z. Wu, W. Lei, K. Xia, H. L. Xin and D. Wang, *ACS Appl. Mater. Interfaces*, 2017, **9**, 26134–26142.
32 Y. Lian, H. Sun, X. Wang, P. Qi, Q. Mu, Y. Chen, J. Ye, X. Zhao, Z. Deng and Y. Peng, *Chem. Sci.*, 2019, **10**, 464–474.
33 Y. Fang, X.-Y. Yu and X. W. Lou, *Adv. Mater.*, 2018, **30**, 1706668.
34 J.-Y. Xie, Z.-Z. Liu, J. Li, L. Feng, M. Yang, Y. Ma, D.-P. Liu, L. Wang, Y.-M. Chai and B. Dong, *J. Energy Chem.*, 2020, **48**, 328–333.
35 V. Ganesan, S. Lim and J. Kim, *Chem. – Asian J.*, 2018, **13**, 413–420.
36 C. Tang, L. Gan, R. Zhang, W. Lu, X. Jiang, A. M. Asiri, X. Sun, J. Wang and L. Chen, *Nano Lett.*, 2016, **16**, 6617–6621.
37 J. Han, G. Chen, X. Liu, N. Zhang, S. Liang, R. Ma and G. Qiuc, *Chem. Commun.*, 2019, **55**, 9212–9215.
38 F. Li, Y. Bu, Z. Lv, J. Mahmood, G.-F. Han, I. Ahmad, G. Kim, Q. Zhong and J.-B. Baek, *Small*, 2017, **13**, 1701167.
39 X. Lv, Z. Hu, J. Ren, Y. Liu, Z. Wang and Z.-Y. Yuan, *Inorg. Chem. Front.*, 2019, **6**, 74–81.
40 M. Zhu, Y. Zhou, Y. Sun, C. Zhu, L. Hu, J. Gao, H. Huang, Y. Liu and Z. Kang, *Dalton Trans.*, 2018, **47**, 5459–5464.
41 A. Mendoza-Garcia, D. Sub and S. Sun, *Nanoscale*, 2016, **8**, 3244–3247.

42 B. Qiu, L. Cai, Y. Wang, Z. Lin, Y. Zuo, M. Wang and Y. Chai, *Adv. Funct. Mater.*, 2018, **28**, 1706008.
43 H. Zhang, W. Zhou, J. Dong, X. F. Lu and X. W. Lou, *Energy Environ. Sci.*, 2019, **12**, 3348–3355.
44 J. Wang, J. Wang, M. Zhang, S. Li, R. Liu and Z. Li, *J. Alloys Compd.*, 2020, **821**, 153463.
45 X. Wang, J. Feng, Y. Bai, Q. Zhang and Y. Yin, *Chem. Rev.*, 2016, **116**, 10983–11060.
46 L.-M. Cao, Y.-W. Hu, S.-F. Tang, A. Iljin, J.-W. Wang, Z.-M. Zhang and T.-B. Lu, *Adv. Sci.*, 2018, **5**, 1800949.
47 Y. Lian, H. Sun, X. Wang, P. Qi, Q. Mu, Y. Chen, J. Ye, X. Zhao, Z. Deng and Y. Peng, *Chem. Sci.*, 2019, **10**, 464–474.
48 J. Shi, F. Qiu, W. Yuan, M. Guo and Z.-H. Lu, *Chem. Eng. J.*, 2021, **403**, 126312.
49 C. Du, L. Yang, F. Yang, G. Cheng and W. Luo, *ACS Catal.*, 2017, **7**, 4131–4137.
50 S. Yue, S. Wang, Q. Jiao, X. Feng, K. Zhan, Y. Dai, C. Feng, H. Li, T. Feng and Y. Zhao, *ChemSusChem*, 2019, **12**, 4461–4470.
51 R. Cai, H. Jin, D. Yang, K.-T. Lin, K. Chan, J. Sun, Z. Chen, X. Zhang and W. Tan, *Nano Energy*, 2020, **17**, 104542.
52 T. Yang, L. Yin, M. He, W. Wei, G. Cao, X. Ding, Y. Wang, Z. Zhao, T. Yu, H. Zhaoa and D. Zhang, *Chem. Commun.*, 2019, **55**, 14343–14346.
53 G. Mei, H. Liang, B. Wei, H. Shi, F. Ming, X. Xu and Z. Wang, *Electrochim. Acta*, 2018, **290**, 82–89.